Granular avalanches across irregular three-dimensional terrain: 1. Theory and computation

Roger P. Denlinger and Richard M. Iverson
U.S. Geological Survey, Vancouver, Washington, USA

Received 29 August 2003; revised 22 January 2004; accepted 29 January 2004; published 27 March 2004.

[1] To establish a theoretical basis for predicting and interpreting the behavior of rapid mass movements on Earth's surface, we develop and test a new computational model for gravity-driven motion of granular avalanches across irregular, three-dimensional (3-D) terrain. The principles embodied in the model are simple and few: continuum mass and momentum conservation and intergranular stress generation governed by Coulomb friction. However, significant challenges result from the necessity of satisfying these principles when deforming avalanches interact with steep and highly variable 3-D terrain. We address these challenges in four ways. (1) We formulate depth-averaged governing equations that are referenced to a rectangular Cartesian coordinate system (with z vertical) and that account explicitly for the effect of nonzero vertical accelerations on depth-averaged mass and momentum fluxes and stress states. (2) We compute fluxes of mass and momentum across vertical cell boundaries using a high-resolution finite volume method and Roe-type Riemann solver. Our algorithm incorporates flux difference splitting, an entropy correction for the flux, and eigenvector decomposition to embed the effects of driving and resisting forces in Riemann solutions. (3) We use a finite element method and avalanche displacements predicted by Riemann solutions to compute Coulomb stresses conjugate to the displacements in 3-D stress space. (4) We test the model output against analytical solutions, a sand cone conceptual experiment, and (in a companion paper) data from detailed laboratory experiments. Model results illustrate a complex interplay of basal traction and internal stress, and they successfully predict not only the gross behavior but also many details of avalanche motion from initiation to deposition. *INDEX TERMS:* 1824 Hydrology: Geomorphology (1625); 3210 Mathematical Geophysics: Modeling; 1815 Hydrology: Erosion and sedimentation; 8020 Structural Geology: Mechanics; 8168 Tectonophysics: Stresses—general; *KEYWORDS:* geomorphology, avalanche, granular experiments, landslide, model, three-dimensional

Citation: Denlinger, R. P., and R. M. Iverson (2004), Granular avalanches across irregular three-dimensional terrain: 1. Theory and computation, *J. Geophys. Res.*, *109*, F01014, doi:10.1029/2003JF000085.

1. Introduction

[2] Understanding of granular avalanches provides a foundation for understanding a variety of mass movement phenomena, including rock avalanches, snow avalanches, debris flows, and pyroclastic flows. These phenomena typically involve mixtures of solid grains and intergranular fluid that surge rapidly across irregular terrain, but granular avalanches constitute an important end-member case, in which intergranular fluid and cohesion play negligible roles. The relative simplicity of this special case makes it a compelling target for development and testing of physically based predictive models. Rigorous formulation and stringent testing of granular avalanche models provide the scientific underpinnings for modeling diverse mass movements on the Earth and other planets.

[3] In this paper we describe an approach to modeling granular avalanches that both extends and revises an approach pioneered by *Savage and Hutter* [1989, 1991]. Our central postulate parallels that of *Savage and Hutter* [1989, 1991] and holds that granular avalanches behave as shallow, isochoric flows of finite volumes of continuous media in which mass and momentum are conserved and shear and normal stresses on internal and bounding surfaces obey the *Coulomb* [1776] friction equation ($\tau = \sigma \tan \phi$, where τ and σ are the shear and normal stresses on failure surfaces with friction angle ϕ). Experiments demonstrate that applicability of the Coulomb equation extends beyond the quasistatic flow regime, in which grains interact exclusively through enduring frictional contacts, because even rapid granular flows exhibit a Coulomb-like proportionality between shear and normal stresses [e.g., *Bagnold*, 1954; *Hungr and Morgenstern*, 1984; *Savage and Hutter*, 1989; *Iverson and Denlinger*, 2001; *Hunt et al.*, 2002]. Elaborate constitutive postulates appear unnecessary in avalanche models unless compelling data indicate that the simple Coulomb postulate is inadequate.

[4] The decade following the publications of *Savage and Hutter* [1989, 1991] witnessed an expansion and general-

ization of their approach. Key elements of the original work by *Savage and Hutter* [1989, 1991] included (1) derivation and scaling of depth-averaged momentum and mass conservation equations to obtain one-dimensional shallow flow equations appropriately normalized to account for the finite size of avalanching masses; (2) formulation of shallow flow equations using the Coulomb equation for basal shear resistance and an earth-pressure equation for the influence of Coulomb friction on longitudinal normal stresses; (3) numerical solution of the one-dimensional shallow flow equations using a Lagrangian finite difference scheme suitable for tracking propagation and deformation of an avalanching mass; and (4) experimental testing that demonstrated the veracity of the model. Subsequent generalizations of the Savage-Hutter approach have included extension to multidimensional avalanches [*Hutter et al.*, 1993; *Gray et al.*, 1999; *Denlinger and Iverson*, 2001; *Pudasaini and Hutter*, 2003], extension to flows containing viscous intergranular fluid [*Iverson*, 1997; *Iverson and Denlinger*, 2001; *Savage and Iverson*, 2003], and a variety of numerical implementations and experimental tests [e.g., *Hutter and Koch*, 1991; *Wieland et al.*, 1999; *Denlinger and Iverson*, 2001; *Gray et al.*, 1999]. As a consequence, the Savage-Hutter approach has incrementally advanced to a stage in which reliable application to complex geophysical phenomena appears within reach.

[5] Here we focus on one of the biggest challenges in extending the Savage-Hutter approach to geophysical applications: assessment of avalanche behavior when motion is affected by irregular, three-dimensional terrain. The strong influence of irregular terrain on geophysical flows is clearly evident. For example, topographic steering dramatically affected the catastrophic $\sim$2.5 km^3 rockslide-debris avalanche at Mount St. Helens, Washington, in 1980 [*Voight et al.*, 1983; *Glicken*, 1998]. In one location, part of the advancing avalanche front surmounted the 300-m-high Johnston Ridge, while the remainder of the avalanche was deflected by the ridge and redirected almost 90° into the Toutle River valley. As at Mount St. Helens, the terrain in most locations prone to catastrophic avalanches is steep and irregular, and abrupt changes in slope angle and orientation over distances much less than typical avalanche dimensions are common. Therefore it is crucial to account for multidimensional momentum transfer within avalanches and for the influence of three-dimensional reaction forces exerted by the underlying Earth.

[6] Although prior calculations have addressed the effects of three-dimensional basal topography on granular avalanches, these calculations have involved restrictive assumptions about the orientation of Coulomb stresses [e.g., *Gray et al.*, 1999; *Denlinger and Iverson*, 2001]. Moreover, tests of the accuracy of these calculations have employed only gently curving, regular terrain that is far less complex than that of most natural landscapes. Rigorous analysis and testing of the effects of irregular terrain has been lacking but is required before geophysical applications can be undertaken with confidence.

[7] The investigations we report here are novel in three respects. First, we develop a new, quasi three-dimensional algorithm for resolving arbitrarily oriented Coulomb stresses in a model of shallow flow across arbitrarily complex terrain. Second, we solve the shallow flow equations numerically using a hybrid finite element/finite volume scheme, in which normal-stress effects are embedded in an approximate Riemann solver using a wave propagation algorithm that facilitates accurate computation of both static and dynamic states. Third, in a companion paper we test numerical predictions against data obtained from unique laboratory experiments, in which laser cartography enabled precise determination of the transient geometry of granular avalanches traversing irregular terrain [*Iverson et al.*, 2004]. Further discussion of the origins and geophysical motivation of this work can be found in previous work [*Iverson*, 1997; *Iverson et al.*, 1997; *Denlinger and Iverson*, 2001; *Iverson and Denlinger*, 2001; *Iverson and Vallance*, 2001]. These publications also address the effects of intergranular pore fluid, which we neglect in this paper in order to focus on the effects of complex basal topography.

2. Mathematical Model

2.1. Conceptual Framework

[8] Our depth-averaged mass and momentum conservation equations are similar to those derived previously by *Gray et al.* [1999] and *Iverson and Denlinger* [2001]. However, those authors referenced their equations to a curvilinear coordinate system fitted to basal topography, whereas we reference our equations to a rectangular Cartesian coordinate system, in which the z coordinate is vertical and aligned with the gravitational attraction of the Earth. Our motivation for using this coordinate system is threefold. (1) Flow interaction with irregular topography may cause the direction of velocity vectors to deviate significantly from directions parallel to the local bed surface (e.g., as occurs along steep channel margins). Therefore the direction normal to the bed (a coordinate in the curvilinear system) does not necessarily provide a preferred direction for depth averaging. (2) In a fitted, curvilinear coordinate system, variations in bed orientation imply three-dimensional variations both in the orientation of adjacent computational cells and in their common boundaries and cause problems in balancing numerical fluxes of conserved variables (mass and momentum) between adjacent cells using Riemann methods. (3) Topographic data for natural landscapes are widely available in the form of digital elevation models (DEMs), which provide gridded elevations referenced to a geodetic (Earth-centered) datum. Models for forecasting the behavior of geophysical flows should ideally utilize these gridded elevation data without preprocessing to map the data to a new coordinate system and without postprocessing to interpret the results.

[9] Use of rectangular Cartesian coordinates in our shallow flow model poses some difficulties, however, because acceleration in the vertical (z) direction is not always negligible and basal tractions are not always exerted on a plane normal to z. We address these difficulties by adopting a new and comprehensive strategy for computing Coulomb stresses, which is detailed in section 3.2. A key element of the stress computation involves use of kinematic constraints to estimate time- and space-dependent accelerations in the z direction. These accelerations are used to derive the total vertical acceleration from the z momentum equation, and this acceleration affects both internal stresses and basal tractions. A finite element calculation allows us to stipulate

that these stresses and tractions must map on the surface of a three-dimensional stress-space representation of a Coulomb failure envelope. Computationally, this mapping is simpler to implement than in traditional quasistatic plasticity models because deformation that generates the Coulomb stress state is inertially driven and largely inherited from the preceding time step.

[10] Previous extensions of the Savage-Hutter theory to multidimensional flow have used schemes for incorporating Coulomb stresses that were less comprehensive than the scheme described above. For example, *Hutter et al.* [1993] and *Gray et al.* [1999] used Rankine-state earth-pressure calculations to define anisotropic lateral stress coefficients that specified ratios between lithostatic stresses normal to the bed and depth-averaged normal stresses parallel to the bed. The lateral stress coefficients assumed one of several discrete values commensurate with compressional and extensional deformation in the bed-parallel (x and y) directions. *Iverson and Denlinger* [2001] used a different approach, in which a single, isotropic lateral stress coefficient was specified for the x and y directions (with the lateral stress value contingent on whether the two-dimensional flow was convergent or divergent at a point). Then, Coulomb shear stresses on x-z and y-z planes were evaluated explicitly by inferring that isotropic normal stresses in the x and y direction equaled the mean stress. Although this approach was rotationally invariant in a mathematical sense, the implied stress state retained dependence on the orientation of the x and y coordinates, and in this sense the approach shared a limitation with the approach of *Hutter et al.* [1993] and *Gray et al.* [1999]. Both of these approaches can yield spurious dependence on the coordinate system when solutions for flow across irregular topography are computed. For that reason we have devised a new approach, in which the estimated Coulomb stress state is independent of the orientation of the coordinate system.

2.2. Conservation Laws

[11] To model avalanche motion, we employ integral equations for mass and momentum balances written in the conservative forms [e.g., *Aris*, 1962]

$$\int_V \left[\frac{\partial \rho}{\partial t} + \nabla \cdot \rho \mathbf{u}\right] dV = 0 \tag{1}$$

$$\int_V \left[\frac{\partial (\rho \mathbf{u})}{\partial t} + \nabla \cdot \rho \mathbf{u}\mathbf{u}\right] dV = -\int_V (\nabla \cdot \tau) dV + \int_V \rho \mathbf{g} dV, \tag{2}$$

where V is an arbitrary control volume, t is time, ρ is the bulk density of the granular mass, $\mathbf{g}$ is the gravitational acceleration vector, $\boldsymbol{\tau}$ is the stress tensor, $\mathbf{u}$ is the velocity vector, and $\mathbf{uu}$ is a dyadic product formed from velocity vectors. For stresses we adopt the sign convention that compression is positive, as is customary in soil and rock mechanics [cf. *Iverson and Denlinger*, 2001].

[12] To obtain depth-averaged forms of equations (1) and (2), we stipulate that each control volume V spans the thickness of the granular mass (where this thickness is nonzero) and is referenced to a rectangular Cartesian coordinate system. The volume integrals in equations (1) and (2) are then expressed as

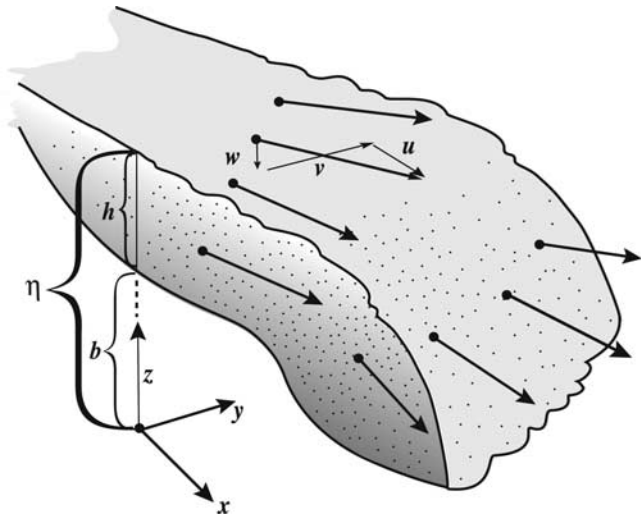

Figure 1. Definition sketch illustrating the coordinate system and variables used to calculate avalanche motion.

$$\int_V dV = \int_A \int_b^\eta dz dA, \tag{3}$$

where A is an area element in the horizontal (x-y) plane, z is the vertical coordinate normal to this plane, $z = b(x, y)$ defines the elevation of the base of the flow, and $z = \eta(x, y, t)$ defines the elevation of the flow surface (Figure 1). We stipulate that no flux of mass occurs across the surfaces $z = b(x, y)$ and $z = \eta(x, y, t)$, which implies that the vertical velocity component w at these surfaces obeys the kinematic boundary conditions

$$[w]_{z=\eta} = \left[\frac{\partial \eta}{\partial t} + u\frac{\partial \eta}{\partial x} + v\frac{\partial \eta}{\partial y}\right]_{z=\eta} \tag{4}$$

$$[w]_{z=b} = \left[u\frac{\partial b}{\partial x} + v\frac{\partial b}{\partial y}\right]_{z=b}, \tag{5}$$

where u and v are the velocity components in the x and y directions, respectively. Note that equations (4) and (5) imply that the z component of velocity (and momentum) is zero only if the avalanche translates across a horizontal surface as a rigid body. We address some ramifications of this fact in our description of stress calculations.

[13] Although the bulk density of deforming granular masses can vary as a consequence of dilation and contraction, such variations are generally slight in comparison to variations in other dynamic properties [cf. *Savage and Hutter*, 1989; *Iverson et al.*, 2000], and we therefore assume ρ is constant. Then, use of equations (1)–(5) and Leibniz theorem for interchanging the order of integration and differentiation [*Abramowitz and Stegun*, 1964, p. 11] enables the conservation equations for mass and momentum to

be expressed in depth-averaged forms analogous to those of shallow water theory:

$$\int_A \left[\frac{\partial h}{\partial t} + \frac{\partial (h\overline{u})}{\partial x} + \frac{\partial (h\overline{v})}{\partial y}\right] dA = 0, \tag{6}$$

$$\rho \int_A \left[\frac{\partial (h\overline{u})}{\partial t} + \frac{\partial (h\overline{u}^2)}{\partial x} + \frac{\partial (h\overline{u}\,\overline{v})}{\partial y}\right] dA = -\int_V \left[\frac{\partial \tau_{xx}}{\partial x} + \frac{\partial \tau_{yx}}{\partial y} + \frac{\partial \tau_{zx}}{\partial z}\right] dV, \tag{7}$$

$$\rho \int_A \left[\frac{\partial (h\overline{v})}{\partial t} + \frac{\partial (h\overline{v}^2)}{\partial y} + \frac{\partial (h\overline{u}\,\overline{v})}{\partial x}\right] dA = -\int_V \left[\frac{\partial \tau_{yy}}{\partial y} + \frac{\partial \tau_{xy}}{\partial x} + \frac{\partial \tau_{zy}}{\partial z}\right] dV, \tag{8}$$

$$\rho \int_A \left[\frac{\partial (h\overline{w})}{\partial t} + \frac{\partial (h\overline{u}\,\overline{w})}{\partial x} + \frac{\partial (h\overline{v}\,\overline{w})}{\partial y}\right] dA = -\int_V \left[\frac{\partial \tau_{zz}}{\partial z} + \frac{\partial \tau_{xz}}{\partial x} + \frac{\partial \tau_{yz}}{\partial y}\right] dV - \int_V \rho g\, dV, \tag{9}$$

where $h = \eta - b$ is the flow thickness, measured vertically from the bed at $z = b$ to the flow surface at $z = \eta$, $\overline{u}$, $\overline{v}$, and $\overline{w}$ are velocity components in the x, y, and z directions, averaged over the thickness h, τ_{ij} are Cartesian components of the stress tensor, and g is the magnitude of the gravitational acceleration **g** in equation (2). As in previous shallow flow theories for granular avalanches, equations (7)–(9) ignore the possible effects of differential advection of momentum due to variation of velocity with depth. (*Vreugdenhil* [1994] provides a detailed discussion of differential advection in the context of shallow water theory.) Inclusion of a correction coefficient to represent the effects of differential advection appears unnecessary for granular avalanches, in which shear deformation tends to be strongly localized near the bed [*Savage and Hutter*, 1989].

2.3. Vertical Stress Calculation

[14] In all shallow flow theories, stress calculations are built around a simplifying assumption regarding the vertical (i.e., z) momentum balance of equation (9). Typically, such theories assume that forces associated with changes in z momentum are negligible relative to the static weight of the mass so that equation (9) reduces to an equation for the z direction static normal stress, $\tau_{zz} = \rho g(\eta - z)$ [cf. *Vreugdenhil*, 1994]. In our theory we use a more general approach that incorporates the influence of changes in z momentum. We have found that this generalization is crucial for computing stresses that are generated by avalanche interaction with irregular terrain.

[15] Mathematically, the rationale for our approach derives from scaling considerations and rearrangement of the z momentum equation (9). Following *Savage and Hutter* [1989] and many subsequent researchers, we note that the length scale for the z direction is the typical avalanche thickness H, whereas the length scale L in the x and y directions is the square root of the typical planimetric area of the avalanche. Typically, $H \ll L$ so that the parameter $\varepsilon = H/L$ is much less than unity. Because all stress components on the right-hand side of equation (9) scale with the lithostatic stress ρgH, we infer that the term $\partial\tau_{zz}/\partial z$ is of the order of ρg, whereas the terms $\partial\tau_{xz}/\partial x$ and $\partial\tau_{yz}/\partial y$ are of the order of $\varepsilon\rho g$ and are small in comparison to $\partial\tau_{zz}/\partial z$. Neglecting these small terms, employing equation (3), evaluating the integral $\int_b^\eta (\partial\tau_{zz}/\partial z)dz$, and utilizing the stress-free surface boundary condition $\tau_{zz}(\eta) = 0$, we reduce equation (9) to an expression for the z direction normal stress at $z = b$:

$$\tau_{zz}(b) = \rho g h + \rho\left[\frac{\partial (h\overline{w})}{\partial t} + \frac{\partial (h\overline{u}\,\overline{w})}{\partial x} + \frac{\partial (h\overline{v}\,\overline{w})}{\partial y}\right]. \tag{10}$$

The right-hand side of equation (10) can be simplified by subtracting the product of $\overline{w}$ and the depth-averaged mass conservation equation (i.e., $\overline{w}\,[\partial h/\partial t + \partial(h\overline{u})/\partial x + \partial(h\overline{v})/\partial y] = 0$) from the term in brackets. As a result, equation (10) can be rewritten as

$$\tau_{zz}(b) = \rho h(g + d\overline{w}/dt), \tag{11}$$

where $d\overline{w}/dt$ denotes the total time derivative $d/dt = \partial/\partial t + \overline{u}\,(\partial/\partial x) + \overline{v}\,(\partial/\partial y)$ of the depth-averaged vertical velocity $\overline{w}$. Finally, by assuming that τ_{zz} varies linearly from $\tau_{zz}(b)$ at the base of the flow to 0 at the free surface, where $z = \eta$, we infer that the z direction normal stress obeys

$$\tau_{zz} \approx \rho g'(\eta - z), \tag{12}$$

where g' is the total vertical acceleration defined by

$$g' = g + d\overline{w}/dt. \tag{13}$$

[16] The concept of total vertical acceleration g' is useful because it indicates that the effect of $d\overline{w}/dt$ on τ_{zz} as defined in equations (12) and (13) either amplifies or reduces the effect of gravity when the flow is vertically accelerated or deflected by topography. For example, a mass that is static or moving with constant velocity has $g' = g$ because $d\overline{w}/dt = 0$, whereas a mass that accelerates in free fall has $g' = 0$ because $d\overline{w}/dt = -g$, and a mass that decelerates vertically as a result of flow impingement against the bed has $g' > g$ because $d\overline{w}/dt > 0$. Physically, the effect of $d\overline{w}/dt$ in equation (13) is analogous to the summed effect of downslope and centripetal accelerations in avalanche theories that use curvilinear coordinates fitted to topography [e.g., *Gray et al.*, 1999; *Iverson and Denlinger*, 2001], but the mathematical form in equation (13) is more readily employed with complex multidimensional terrain.

[17] We use kinematic constraints to estimate the depth-averaged vertical velocity $\overline{w}(x, y, t)$ in equations (11) and (13). Neglecting the effects of differential advection, we infer that $u \approx \overline{u}$ and $v \approx \overline{v}$ are suitable approximations in the kinematic boundary conditions (4) and (5). We also assume that the depth average of w is approximated well by the mean of the surface and basal values of w as given by equations (4) and (5). This mean value,

$$\overline{w} \approx \frac{1}{2}\left[\frac{\partial \eta}{\partial t} + \overline{u}\frac{\partial \eta}{\partial x} + \overline{v}\frac{\partial \eta}{\partial y}\right] + \frac{1}{2}\left[\overline{u}\frac{\partial b}{\partial x} + \overline{v}\frac{\partial b}{\partial y}\right], \tag{14}$$

is used to compute the total vertical acceleration defined in equation (13). The connection between equation (13), equation (14), and the concept of total vertical acceleration can be clarified by considering simple cases that yield analytical solutions, as in Appendix A.

[18] As in previous granular avalanche theories that build upon the theory of *Savage and Hutter* [1989], we assume that lateral normal stresses are proportional to τ_{zz}; that is,

$$\tau_{xx} = k_x \tau_{zz} \qquad \tau_{yy} = k_y \tau_{zz}, \tag{15}$$

where k_x and k_y are lateral stress coefficients that have values derived from Coulomb stress calculations. However, whereas previous theories have assumed that k_x and k_y have one of several discrete values dictated by Rankine-state calculations for extending or compressing quasistatic deformation of uniform Coulomb slabs, our quasi three-dimensional finite element calculations yield continuously varying k_x and k_y values that depend on all components of the stress and flow fields. This approach yields improved resolution of Coulomb stresses and smooth variations in these stresses from cell to cell, even where avalanches interact with abrupt changes in topography. Implementation of our finite element calculation is outlined in section 3.2.

[19] The physical significance of the lateral stress coefficients k_x and k_y defined in equation (15) and of g' defined in equation (13) becomes more apparent when equation (12) is substituted into equation (15), equation (15) is substituted into equations (7) and (8), and the stress integrals on the right-hand sides of equations (7) and (8) are evaluated. For example, with these substitutions the right-hand side of the x momentum equation (7) reduces to

$$\int_V \left[\frac{\partial \tau_{xx}}{\partial x} + \frac{\partial \tau_{yx}}{\partial y} + \frac{\partial \tau_{zx}}{\partial z}\right] dV = \int_A \int_b^{\eta} \frac{\partial [k_x \rho g'(\eta - z)]}{\partial x} dz dA + \int_V \frac{\partial \tau_{yx}}{\partial y} dV - \int_A \tau_{zx}(b) dA. \tag{16}$$

The final term on the right-hand side of this equation results from employing equation (3) and integrating from $z = b$ to $z = \eta$. The depth integral involving the lateral normal stress $k_x \rho g'(\eta - z)$ can be evaluated explicitly using Leibniz's theorem, which yields

$$\int_b^{\eta} \frac{\partial [k_x \rho g'(\eta - z)]}{\partial x} dz = \rho g' h k_x \left[\frac{\partial b}{\partial x} + \frac{\partial h}{\partial x}\right] + \frac{1}{2} h^2 \rho \left[g' \frac{\partial k_x}{\partial x} + k_x \frac{\partial g'}{\partial x}\right]. \tag{17}$$

As described by equation (17), the transmission of normal stress in the x direction depends not only on the bed slope and thickness gradient (as it would in a typical shallow water flow) but also on $k_x g'$ and the gradients of k_x and g'. Indeed, as shown by *Denlinger and Iverson* [2001], it is useful to combine the influences of all these factors to define a gravity wave speed $\sqrt{k_x g' h}$ that describes the maximum rate of information propagation in the avalanche. Unlike *Denlinger and Iverson* [2001], however, we emphasize here that the gravity wave speed includes the total vertical acceleration as defined in equation (13).

[20] Expressions analogous to equations (16) and (17) are easily obtained and applied for the y momentum equation, and all these expressions are used in the vector form of the conservation equations presented below.

3. Numerical Method

[21] Our numerical technique for solving the depth-averaged conservation equations (6)–(8) utilizes a hybrid finite volume/finite element procedure. The key advantages of this technique are twofold: (1) the finite volume method is very effective for preserving conservation of mass and momentum in multidimensional physical systems such as granular avalanches, wherein abrupt transitions between rapidly flowing and stationary states are common [e.g., *LeVeque*, 2002; *Toro*, 1997]; (2) the finite element method is a powerful means of resolving Coulomb stress states when flow is oriented arbitrarily with respect to an imposed coordinate system. Finite volume calculations of fluxes of mass and momentum provide kinematic constraints for finite element calculations of stresses, and the finite element stress calculations in turn provide a basis for evaluating source terms that modify fluxes.

[22] As a preliminary step in our numerical method, we break the flow domain into discrete cells with vertical boundaries, through which fluxes of mass and momentum pass during each increment in time. Evaluation of fluxes is accomplished by rewriting equations (6)–(8) in the vector form

$$\int_A \frac{\partial \mathbf{Q}}{\partial t} dA + \int_A \frac{\partial \mathbf{F}}{\partial x} dA + \int_A \frac{\partial \mathbf{G}}{\partial y} dA = \int_A \mathbf{S}_g dA + \mathbf{S}_\tau, \tag{18}$$

where $\mathbf{Q}$ is the vector of conserved flow variables:

$$\mathbf{Q} = \begin{pmatrix} h \\ hu \\ hv \end{pmatrix}. \tag{19}$$

Here, and in all equations that follow, overbars are omitted from the velocity components u and v, but these symbols continue to denote depth-averaged quantities. In equation (18) the vectors $\mathbf{F}$ and $\mathbf{G}$ describe the flux of mass and momentum in the x and y directions, respectively, $\mathbf{S}_g$ contains gravitational driving or "source" terms, and $\mathbf{S}_\tau$ contains the source terms resulting from internal stresses and boundary forces on the right-hand sides of equations (7) and (8). Specifically, we have

$$\mathbf{F} = \begin{pmatrix} hu \\ hu^2 + \frac{1}{2} k_x g' h^2 \\ huv \end{pmatrix}, \tag{20}$$

$$\mathbf{G} = \begin{pmatrix} hv \\ huv \\ hv^2 + \frac{1}{2} k_y g' h^2 \end{pmatrix}, \tag{21}$$

$$\mathbf{S}_g = \begin{pmatrix} 0 \\ k_x g' h \frac{\partial b}{\partial x} + \frac{1}{2} g' h^2 \frac{\partial k_x}{\partial x} \\ k_y g' h \frac{\partial b}{\partial y} + \frac{1}{2} g' h^2 \frac{\partial k_y}{\partial y} \end{pmatrix}, \tag{22}$$

$$\mathbf{S}_\tau = \begin{pmatrix} 0 \\ \int_V \frac{\partial \tau_{yx}}{\partial y} dV - \int_A \tau_{zx}(b) dA \\ \int_V \frac{\partial \tau_{xy}}{\partial x} dV - \int_A \tau_{zy}(b) dA \end{pmatrix}. \quad (23)$$

The conservation equations (18) are solved using stresses from the previous time step in $\mathbf{S}_g$ and $\mathbf{S}_\tau$. Once a flow solution is obtained, finite element methods are used to calculate internal stresses and to modify these source terms for the next time step.

3.1. Finite Volume Method For Flow Calculation

[23] In the finite volume method the area integrals of $\partial\mathbf{F}/\partial x$ and $\partial\mathbf{G}/\partial y$ are replaced by line integrals of the net flux across the vertical boundaries of each cell, as discussed by *LeVeque* [2002, p. 422]. To update the flow variables in each cell to the next time step, we use a forward Euler discretization of equation (18) between time t^n and time t^{n+1} to give the conservative difference scheme

$$\mathbf{Q}^{n+1} = \mathbf{Q}^n - \frac{\Delta t}{V_{ij}} \sum_{k=1}^{N_e} L_{ik} \cdot (\mathbf{F}_{ik} \cdot \mathbf{n}_{ik} + \mathbf{G}_{ik} \cdot \mathbf{n}_{ik}) + \frac{\Delta t}{V_{ij}} \mathbf{S}_{ij}^*, \quad (24)$$

where the superscripts on $\mathbf{Q}$ denote the time increment, V_{ij} is the volume of cell ij, N_e is the number of cell edges, $\mathbf{n}_{ik}$ is the outward normal of the edge between cell i and cell k, L_{ik} is the length of that edge, and $\mathbf{S}_{ij}^*$ is the combined vector of source term integrals over each cell.

[24] To solve equation (24), we construct Jacobians $\partial\mathbf{F}/\partial\mathbf{Q}$ and $\partial\mathbf{G}/\partial\mathbf{Q}$ of the flux such that their product with the change in $\mathbf{Q}$ across a cell edge is equal to the jump in flux $\Delta\mathbf{F}$ or $\Delta\mathbf{G}$ across that edge. This condition is enforced by using Roe averages of the flow variables (defined below) between cells in these Jacobians [*Roe*, 1981] and by assuming that these averages are constant for the duration of the time step. As the advective terms in our conservation equations (6)–(8) are identical to those in the standard shallow water equations, the Roe averages are given for the x direction by *LeVeque* [2002, p. 481] as

$$\tilde{h} = \frac{h_R + h_L}{2}, \quad (25)$$

$$\tilde{u} = \frac{u_R\sqrt{h_R} + u_L\sqrt{h_L}}{\sqrt{h_R} + \sqrt{h_L}}, \quad (26)$$

$$\tilde{v} = \frac{h_L(\tilde{u} - u_L)v_L + h_R(u_R - \tilde{u})v_R}{h_L(\tilde{u} - u_L) + h_R(u_R - \tilde{u})}. \quad (27)$$

In these equations and all that follow, symbols with tildes denote Roe averages. Analogous equations apply for the $\mathbf{G}$ flux and are obtained by interchanging u and v above.

[25] Constructed with Roe averages, the fluxes $\mathbf{F}$ and $\mathbf{G}$ in equation (24) form a constant coefficient, linear system and consequently, an approximation to the flux at every time step may be obtained in a variety of ways. Here we use a wave propagation form of Godunov's method as outlined by *LeVeque* [2002, p. 78] and represent these flux differences as mathematical waves. We begin by factoring the flux terms into characteristic components of the homogeneous system

$$\frac{\partial\mathbf{Q}}{\partial t} + \tilde{\mathbf{A}}\frac{\partial\mathbf{Q}}{\partial x} + \tilde{\mathbf{B}}\frac{\partial\mathbf{Q}}{\partial y} = 0, \quad (28)$$

where

$$\tilde{\mathbf{A}} = \frac{\partial\tilde{\mathbf{F}}}{\partial\mathbf{Q}} \quad (29)$$

$$\tilde{\mathbf{B}} = \frac{\partial\tilde{\mathbf{G}}}{\partial\mathbf{Q}} \quad (30)$$

are the linear approximations to the Jacobian matrices of the flux in the x and y directions. These Jacobian matrices contain the information needed to solve for mass and momentum fluxes in the flow. The eigenvalues of the Jacobians are real, making the conservation equations fully hyperbolic. Factoring these Jacobian matrices into right and left eigenvector matrices, we decompose the flow vector onto them to determine the fan of flow characteristics across each cell edge [*Hubbard and Garcia-Navarro*, 2000]. Using a similar decomposition, the gravitational source term $\mathbf{S}_g$ and stress source term in $\mathbf{S}_\tau$ are also incorporated into the analysis, as described in equations (34)–(37).

[26] The linear form of the flux Jacobian matrices allows us to decouple the conservation equations, writing the flux difference across each cell interface as the sum of N waves, where N is the number of conservation equations being solved. The flux calculation is particularly straightforward for a quadrilateral grid aligned with Cartesian x and y axes. For the grid in Figure 2 the flux difference across the x interface between cells i, j and $i+1, j$ may be written as

$$\Delta F_{i+1/2,j} = \left(\tilde{\mathbf{A}}\Delta\mathbf{Q}\right)_{i+1/2,j} = \left(\tilde{\mathbf{R}}_\mathbf{A}\tilde{\Lambda}_\mathbf{A}\tilde{\mathbf{R}}_\mathbf{A}^{-1}\Delta\mathbf{Q}\right)_{i+1/2,j} = \sum_{k=1}^{N} \left(\tilde{\alpha}_k\tilde{\lambda}_k\tilde{r}_k\right)_{i+1/2,j}, \quad (31)$$

where ΔF is the jump in flux F across the edge, $\mathbf{R}_\mathbf{A}$ is the matrix of right eigenvectors $\tilde{r}_k$ of $\tilde{\mathbf{A}}$, $\tilde{\mathbf{R}}_\mathbf{A}^{-1}$ is the left eigenvector matrix of $\tilde{\mathbf{A}}$, and $\tilde{\Lambda}_\mathbf{A}$ is the diagonal matrix of eigenvalues $\tilde{\lambda}_k$. The wave strengths $\tilde{\alpha}_k$ are given by $\tilde{\mathbf{R}}_\mathbf{A}^{-1}\Delta\mathbf{Q}$. A similar equation is written for the flux jumps ΔG across the y faces.

[27] We write the jumps in flux across each cell edge as a linear combination of right- and left-going waves and update the cell variables on either side as described by *Hubbard and Garcia-Navarro* [2000] and by *LeVeque* [2002, pp. 80–81]. A preliminary estimate of the updated flow vector is given by

$$Q_{ij}^* = Q_{ij}^n - \frac{\Delta t}{\Delta x}\left[\left(\tilde{\mathbf{R}}_\mathbf{A}\tilde{\Lambda}_\mathbf{A}^-\tilde{\mathbf{R}}_\mathbf{A}^{-1}\Delta\mathbf{Q}\right)_{i+1/2,j} + \left(\tilde{\mathbf{R}}_\mathbf{A}\tilde{\Lambda}_\mathbf{A}^+\tilde{\mathbf{R}}_\mathbf{A}^{-1}\Delta\mathbf{Q}\right)_{i-1/2,j}\right] - \frac{\Delta t}{\Delta y}\left[\left(\tilde{\mathbf{R}}_\mathbf{B}\tilde{\Lambda}_\mathbf{B}^-\tilde{\mathbf{R}}_\mathbf{B}^{-1}\Delta\mathbf{Q}\right)_{i,j+1/2} + \left(\tilde{\mathbf{R}}_\mathbf{B}\tilde{\Lambda}_\mathbf{B}^+\tilde{\mathbf{R}}_\mathbf{B}^{-1}\Delta\mathbf{Q}\right)_{i,j-1/2}\right] + \frac{\Delta t}{A_{ij}}\tilde{\mathbf{S}}_{ij}^*, \quad (32)$$

where

$$\tilde{\Lambda}^\pm = \frac{1}{2}\left(\tilde{\Lambda} \pm |\tilde{\Lambda}|\right). \quad (33)$$

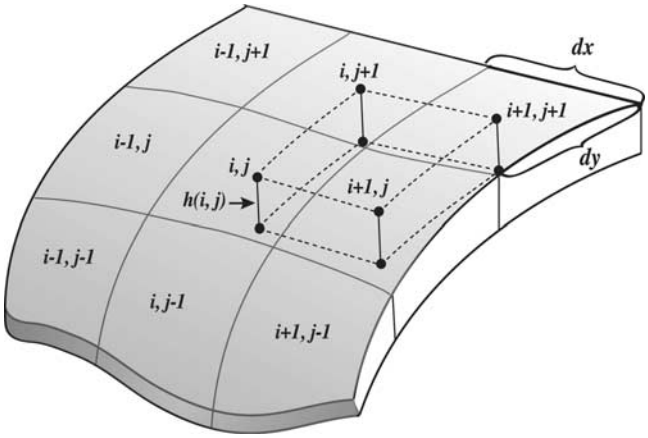

Figure 2. Sample of the offset computational grids used in finite volume computations of fluxes (solid lines) and finite element computations of stresses (dashed lines).

Here $\tilde{\mathbf{R}}_{\mathbf{B}}$ and $\tilde{\mathbf{R}}_{\mathbf{B}}^{-1}$ are the right and left eigenvector matrices of $\tilde{\mathbf{G}}$, respectively, A_{ij} is the area of cell ij, and the splitting of source terms $\tilde{\mathbf{S}}_{ij}^{*}$ will be described below.

[28] Flux difference splitting, treated in equation (32) as waves traveling in opposite directions, produces positive and negative components that are used to split cell edge waves into transverse components, as described by *LeVeque* [2002]. This procedure yields an algorithm that incorporates all nine cells of the labeled stencil shown in Figure 2 to update each grid point, and it thereby minimizes the effects of grid orientation on the solution.

[29] The decomposition of the source terms on vertical cell edges uses the contribution to the source from cells bounding each edge. For example, for the edge between cells i, j and $i + 1, j$ (Figure 2), the source term integration across the cell edge is

$$\int_{j-1/2}^{j+1/2}\int_{i}^{i+1} \tilde{\mathbf{S}}dxdy = \tilde{\mathbf{S}}_{i+1/2,j} = \left(\tilde{\mathbf{R}}\tilde{\mathbf{R}}^{-1}\tilde{\mathbf{S}}\right)_{i+1/2,j} \tag{34}$$

and the x component contributions to the source vector over the entire cell in equation (32) are written

$$\left[\mathbf{S}_{ij}^{*}\right]_{x} = \tilde{\mathbf{S}}_{i+1/2,j}^{-} + \tilde{\mathbf{S}}_{i-1/2,j}^{+}, \tag{35}$$

where

$$\tilde{\mathbf{S}}_{i+1/2,j}^{-} = \frac{1}{2}\left(\tilde{\mathbf{R}}_{\mathbf{A}}\left(\mathbf{I} - \mathrm{sgn}\left(\tilde{\lambda}\right)\right)\tilde{\mathbf{R}}_{\mathbf{A}}^{-1}\tilde{\mathbf{S}}\right)_{i+1/2,j} \tag{36}$$

and

$$\tilde{\mathbf{S}}_{i-1/2,j}^{+} = \frac{1}{2}\left(\tilde{\mathbf{R}}_{\mathbf{A}}\left(\mathbf{I} + \mathrm{sgn}\left(\tilde{\lambda}\right)\right)\tilde{\mathbf{R}}_{\mathbf{A}}^{-1}\tilde{\mathbf{S}}\right)_{i-1/2,j} \tag{37}$$

are the left and right traveling contributions, respectively, with similar terms for the y components. $\mathbf{I}$ is the identity matrix.

[30] The remaining source term (the last term in equation (16)) is not decomposed in this fashion as it represents the basal stress or drag resulting from sliding on the bed. Effects of this bed drag are included in a final computational update, which uses Q_{ij}^{*} of equation (32). The final update is

$$Q_{ij}^{n+1} = Q_{ij}^{*} - \Delta t \cdot \int_{A} (h \cdot \tau_b)_{ij} dA, \tag{38}$$

where A is the cell bed area and the bed drag acts on both components of velocity. Once the updated solution is obtained, the displacements and depths derived from this solution are fixed and then are used to update the stresses for the next time step.

3.2. Finite Element Method For Resolving Coulomb Stresses

[31] We calculate the Coulomb stresses within the granular avalanche using finite element methods in conjunction with the velocities and flow thicknesses obtained from the finite volume solution described in section 3.1. The stresses are estimated at the center of a finite element brick with corner vertices at the centroids of the upper and basal surfaces of four adjoining finite volume cells (Figure 2). The velocities at the base and the surface of each finite volume determine the displacements at a corner of a finite element.

[32] The expression for strain within each finite element is given as

$$\boldsymbol{\varepsilon} = \begin{pmatrix} \varepsilon_{xx} \\ \varepsilon_{yy} \\ \varepsilon_{zz} \\ \varepsilon_{xy} \\ \varepsilon_{yz} \\ \varepsilon_{xz} \end{pmatrix} = \mathbf{L} \cdot \sum_{\text{corners}} \begin{pmatrix} u\Delta t \\ v\Delta t \\ w\Delta t \end{pmatrix}, \tag{39}$$

where $\mathbf{L}$ is a linear differential operator that converts corner displacements (the product of velocity and time step) to strain. An example of this operator is given as $\mathbf{S}$ in the work of *Zienkiewicz and Taylor* [2000, equation (6.9)]. As only corner displacements are specified, strains are regarded as constant within each element.

[33] The stresses resulting from these strains cannot exceed the Coulomb shear strength of the granular material. If shear stresses are less than the Coulomb strength, the material remains elastic and no flow occurs (although sliding can occur at the bed). The stresses accompanying the strains given by equation (39) are initially estimated by

$$\Delta\tau = \mathbf{D}\boldsymbol{\varepsilon}, \tag{40}$$

where the total stress is

$$\boldsymbol{\tau} = \boldsymbol{\tau}^{n} + \Delta\boldsymbol{\tau}. \tag{41}$$

Here $\Delta\boldsymbol{\tau}$ is the current stress increment, $\boldsymbol{\tau}^{n}$ is the preexisting stress at the same location, $\boldsymbol{\varepsilon}$ is the strain tensor on the left hand side of equation (39), and $\mathbf{D}$ is an isotropic matrix of elastic constants [*Zienkiewicz and Taylor*, 2000, equation (6.14)]. This stress estimate is added to other contributions to the stress resulting from sliding along the bed (bed shear stress) and from the material weight.

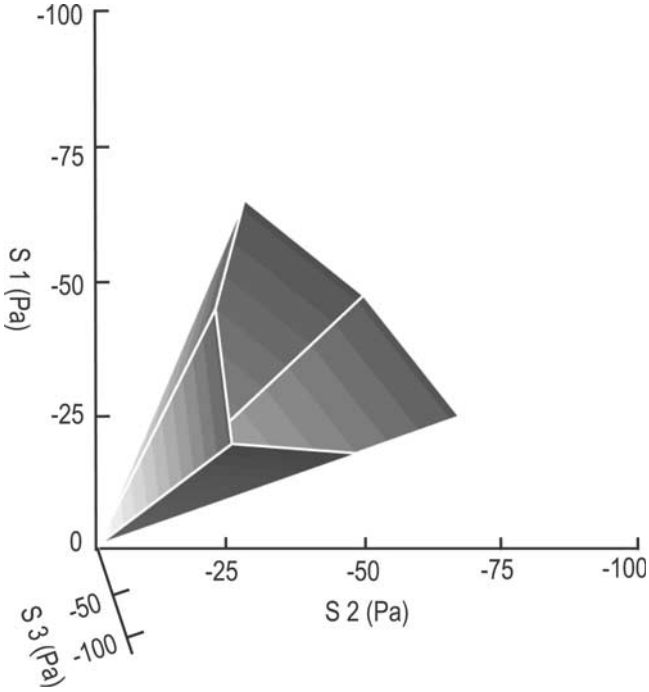

Figure 3. Coulomb yield surface in three-dimensional stress space, where S1, S2, and S3 represent principal stress components of unspecified relative magnitude. A line passing axially through the center of the irregular hexagonal cone forming the yield surface represents a lithostatic state of stress. The yield surface was computed for the sand used in experiment B of *Iverson et al.* [2004].

[34] The bed shear stress is determined from the granular material's weight per unit of bed area and bed orientation relative to the flow or, in a frame of reference oriented parallel to the bed,

$$\tau_{\mathrm{bed}} = \rho g' \gamma_{zz'} h \cdot \tan \phi_{\mathrm{bed}}, \tag{42}$$

where τ_{bed} is the bed shear stress, g' is given by equation (13), and $\gamma_{zz'}$ is the direction cosine of the bed normal with respect to vertical. The bed shear stress in equation (42) is transformed into our Cartesian coordinate system as described in Appendix B and is then added to the weight and to the flow stress of equation (41) to obtain an initial estimate for the total state of stress in the element. If flow occurs, the initial stress state necessarily exceeds the strength as described by the Coulomb yield criterion.

[35] The shear strength defined by the Coulomb criterion is pressure-dependent but not rate-dependent, and Coulomb shear stresses increase with the mean stress. For sand B in our experimental tests [*Iverson et al.*, 2004], the admissible stresses are enclosed by the irregular, hexagonal Coulomb yield cone shown in Figure 3. The cone is hexagonal rather than circular in cross section because yield is determined solely by the difference between the maximum and minimum principal stresses in the flow [*Desai and Siriwardane*, 1984]. The axis of this cone defines a lithostatic stress state, and an infinite number of Mohr stress circles may be inscribed within the cone on planes containing this axis. Inside the cone the differences between principal stresses are insufficient to produce shear failure, whereas outside the cone the principal stress differences are too large to be supported by the material. As the granular material deforms, the stresses remain on the cone surface.

[36] Mathematically, the shift in stresses during a time step must satisfy yield conditions specified by

$$\frac{\partial Y}{\partial \boldsymbol{\tau}} \Delta \boldsymbol{\tau} = 0. \tag{43}$$

For Coulomb behavior the yield function Y is [*Zienkiewicz and Taylor*, 1991]

$$Y = \sigma_m \sin \phi_{\mathrm{int}} + \overline{\sigma}\left(\frac{\cos\theta}{\sqrt{3}} - \frac{\sin\theta \sin\phi_{\mathrm{int}}}{3}\right) - c\cos\phi_{\mathrm{int}}, \tag{44}$$

which is written in terms of stress invariants σ_m, $\overline{\sigma}$, θ, defined as

$$\sigma_m = -\frac{(\tau_{xx} + \tau_{yy} + \tau_{zz})}{3}, \tag{45}$$

$$\overline{\sigma} = \frac{1}{\sqrt{3}}\left[(\tau_{xx} - \tau_{yy})^2 + (\tau_{yy} - \tau_{zz})^2 + (\tau_{xx} - \tau_{zz})^2 + 6\tau_{xy}^2 + 6\tau_{yz}^2 + 6\tau_{xz}^2\right]^{1/2}, \tag{46}$$

$$\theta = \frac{1}{3}\arcsin\left(\frac{3\sqrt{3}}{2}\frac{\det s}{(\overline{\sigma})^3}\right), \tag{47}$$

$$s_{ij} = \tau_{ij} - \sigma_m. \tag{48}$$

Here $\tau_i = \tau_{ii}$ for $i = x, y, z$ and ϕ_{int} is the angle of internal friction. Note that equation (47) is not the conventional third stress invariant commonly used in continuum mechanics but is an alternative invariant written in terms of the deviatoric stress s_{ij} [cf. *Malvern*, 1969].

[37] The correction of the stress from conditions outside the yield surface shown in Figure 3 to the yield surface (Y in equation (44)) is obtained by iteratively solving

$$\Delta \boldsymbol{\tau} = \left(\mathbf{D} - \frac{\mathbf{D}\dfrac{\partial Y'}{\partial \tau}\left(\dfrac{\partial Y}{\partial \tau}\right)^{\mathbf{T}}\mathbf{D}}{\left(\dfrac{\partial Y}{\partial \tau}\right)^{\mathbf{T}}\mathbf{D}\dfrac{\partial Y'}{\partial \tau}}\right) \cdot \varepsilon, \tag{49}$$

where $\boldsymbol{\varepsilon}$ is the strain occurring over the time increment Δt in equation (39) and Y' is the yield function that is assumed to apply outside the yield surface. Here we use the same function as Y, with an internal friction angle of 4°, a value commonly observed in residual friction studies of sand [*Wood*, 1990]. Typically, only a few iterations are required to attain the condition in equation (43).

[38] In our avalanche computations the initial state of stress prior to any deformation is assumed to be lithostatic, where all stresses are equal and determined by the depth at the centroid of each finite element brick. Once deformation begins, the initial elastic stress estimate typically is far outside the yield surface in stress space (Figure 3). Iterating on equation (49), we return the stress state to a position on the Coulomb yield cone (Figure 3). In general, this changes the magnitudes and ratios of all stress components. For a displacement-driven system, as we have here, this process is

robust and accurate, and as the corrections are large, it is insensitive to the values used for the elastic constants. As a final step, the stresses in the surrounding finite elements are averaged to the center of each finite volume cell (Figure 2) to begin the next time increment.

4. Computational Results and Model Verification

[39] We test our model in three ways. (1) Computational accuracy is tested by comparing model predictions with those of appropriate one-dimensional analytical solutions. (2) To test for spurious grid dependence, we compute the symmetrical collapse of cylindrical sand columns to form conical heaps. (3) Finally, to test all aspects of the model against physical reality, we compare computational predictions to results of sand avalanche experiments conducted in a laboratory flume. A complete description of these experiments, together with a complete set of comparisons between model predictions and experimental results, is presented in a companion paper [*Iverson et al.*, 2004]. Here we use the experimental data to illustrate how specific attributes of the model facilitate prediction of complicated, three-dimensional avalanche behavior.

4.1. Analytical Solution

[40] *Mangeney et al.* [2000] provide an analytical solution for a one-dimensional granular avalanche with lithostatic internal stress (and hence zero internal friction) but with significant bed friction. The solution describes motion of a flow front that avalanches off an unsupported face of an infinite slab of material resting on an infinite, uniform slope. Figure 4 depicts the comparison between this analytical solution and our numerical solution for two different values of the bed friction angle and bed slope.

[41] In the first example (Figure 4a), with zero bed slope and zero friction, the equations governing the flow reduce to the standard shallow water equations. In this case, our computational results are identical with the analytical results for sudden release of the vertical front.

[42] The second example (Figure 4b), with a 30° bed slope and a 20° angle of bed friction, is more closely analogous to a typical granular avalanche. This example illustrates the importance of using the total vertical acceleration g' in computations. Here the vertical component of the avalanche acceleration reduces the apparent weight of the granular mass and thereby reduces the basal frictional resistance. If the vertical acceleration is erroneously fixed at the value of g, the basal normal force derived from this value is too large, and excess basal friction causes the numerical solution to lag behind the analytical one. Incorporating the total vertical acceleration in the g' computation brings the numerical solution into close agreement with the analytical solution. The discrepancy at the flow front is the result of using a small, nonzero depth to define the flow front. The minimum cell depth at which momentum is calculated is given by the front height $(1/2)dx \tan \phi_b$, where ϕ_b is the basal friction angle. As the cell size decreases, the discrepancy between the two solutions also decreases.

4.2. Collapse of Sand Cylinder

[43] A numerical experiment emulating the release of a vertical cylinder of water is commonly used to test spreading and grid dependence in multidimensional dam break models [*Guinot*, 2003; *LeVeque*, 2002]. Here we run a similar experiment, but with a vertical cylinder of sand, which unlike water will come to rest as a cone-shaped deposit. The final slope angle of the cone is somewhat less than the sand's angle of repose as friction has to overcome the momentum of the vertical collapse to arrest the flow.

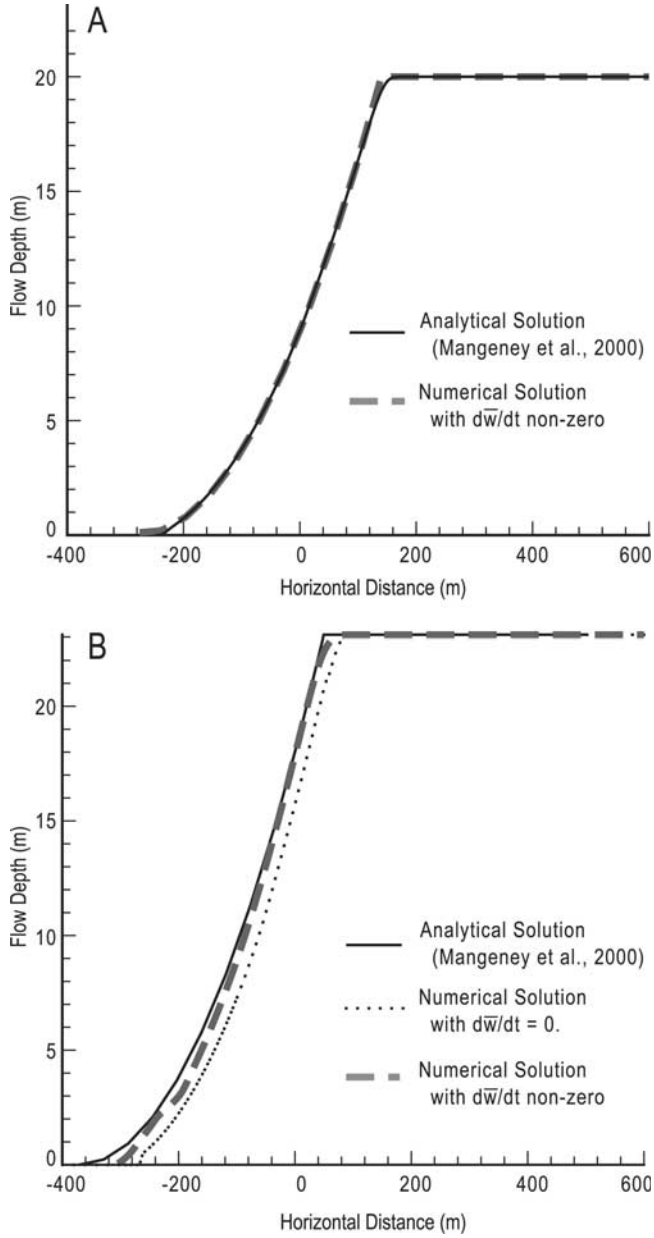

Figure 4. Graphs comparing solutions that predict flow depth as a function of distance and time for a one-dimensional dam break problem. Analytical solutions are from *Mangeney et al.* [2000], and numerical solutions are obtained using our model. (a) Solutions for a tabular reservoir of sand with zero bed slope, zero internal friction, and zero bed friction at a time of 10 s. (b) Solutions for a tabular reservoir of sand with a 30° bed slope, zero internal friction, and 20° basal friction at a time of 15 s. For this case, two numerical solutions are shown, one which uses only g as the vertical acceleration and one which uses the total vertical acceleration, $g' = g + d\overline{w}/dt$.

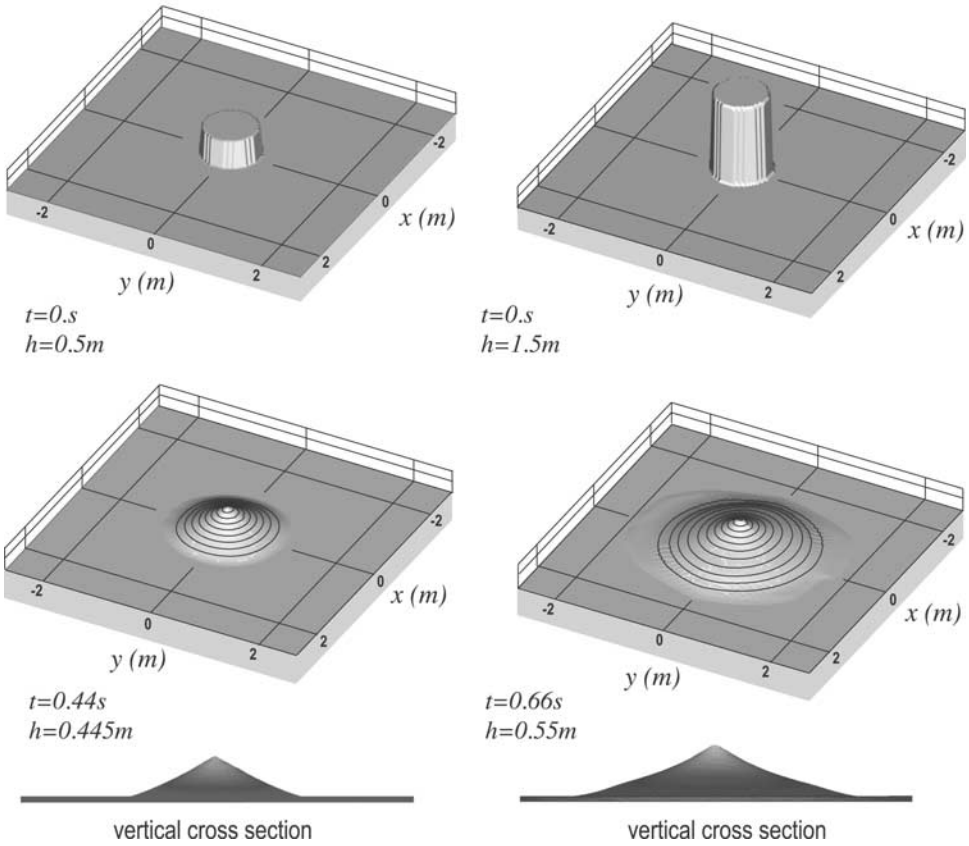

Figure 5. Results of numerical simulations of collapse of vertical cylinders of sand to form cones.

[44] The results shown in Figure 5 test two aspects of the model. First, the deposits that are generated are circular cones with no distortion produced by the quadrilateral grid, reflecting the effectiveness of the transverse splitting of the momentum flux in the model. Second, a taller cylinder generates more vertical momentum, and conversion of this vertical momentum to horizontal momentum through the interaction of basal forces and internal stresses produces a flatter cone. The same results and timing are generated when the grid spacing is reduced by half, lending confidence in the numerical results.

4.3. Experimental Avalanches

[45] Finally, and most importantly, we test our model predictions by comparison with the behavior of avalanches of sand in a laboratory flume with irregular topography. *Iverson et al.* [2004] provide a detailed description of these experimental avalanches as well as comprehensive comparisons between the experimental and computational results. Here we focus on specific aspects of the results that test and illustrate some key attributes of our model. Of particular interest is the shape, speed, and stress distribution of the avalanche front as it interacts with terrain. The speed of the front is directly related to the gravity wave speed and the relationship of internal stresses to basal shear stress.

[46] Figure 6 depicts an avalanche front predicted for a time 0.3 s after the release of experimental avalanche A of *Iverson et al.* [2004]. The front is split by a midchannel ridge as the avalanche funnels into a narrow chute. A surface mesh of the finite elements used to determine stresses, along with avalanche depths and the velocities driving the stress states, are also shown in Figure 6. The vectors depict surface velocities so that where the vectors are not visible, they project under the surface (since the avalanche is extending and becoming thinner as advance of the propagating front outstrips the influx of sand). Smooth variation of these vectors and of the avalanche depth as well as excellent correspondence of the predicted and measured positions of the avalanche front [*Iverson et al.*, 2004] support the viability of our model.

[47] Figure 7 illustrates model predictions of the interplay of depth, velocity, stress, and vertical acceleration $d\overline{w}/dt$ in an advancing avalanche front. For comparison, Figure 7 also depicts a photograph of experimental avalanche B of *Iverson et al.* [2004] at the same instant (0.31 s after avalanche release). The trajectories of black tracer particles visible in the photograph provide an indication of avalanche surface velocities.

[48] Figures 7c and 7d show the distribution of horizontal normal stresses scaled by the vertical stress (τ_{xx}/τ_{zz} and τ_{yy}/τ_{zz}) throughout static and moving parts of the avalanche. The stresses respond strongly to variations in topography that produce localized regions of compression and extension. In some instances the lateral normal stress components are isotropic, whereas in other instances, they are not. This result contrasts with earlier results of *Denlinger and Iverson* [2001]. Moreover, the computed stresses shown in Figure 7 vary continuously and smoothly, in marked contrast with stresses computed using Rankine-state pressure coefficients in previous models [e.g., *Gray et al.*, 1999; *Iverson and Denlinger*, 2001].

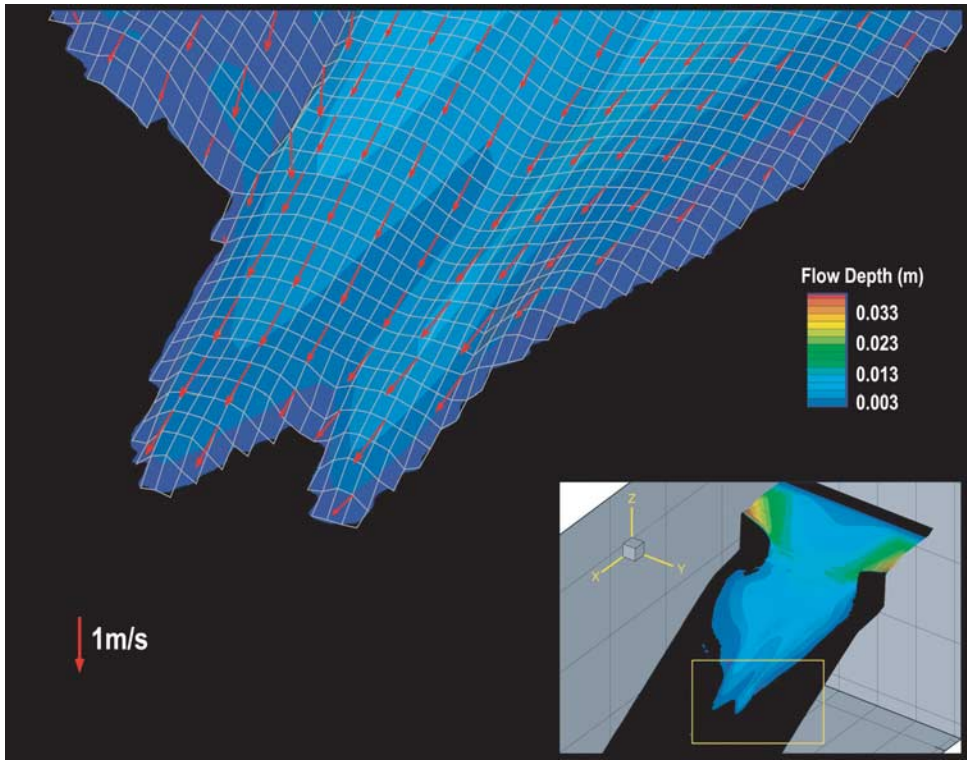

Figure 6. Oblique views of the computed distribution of sand thickness and velocity as an avalanche front discharges from the head of the flume used in experiment A of *Iverson et al.* [2004]. Time is 0.3 s after avalanche release. Velocities vectors (red) depict surface velocities. The computational mesh of cells (in gray) shows the active finite element grid used to estimate stresses.

[49] Figure 7e depicts the vertical acceleration $d\overline{w}/dt$ normalized by the magnitude of gravitational acceleration. The magnitude of $d\overline{w}/dt$ can be comparable to that of gravity, with great ramifications for all components of stress. High values of $d\overline{w}/dt$ occur where descending sand impinges against the bed and low values on steep lee sides of ridges within the bed topography. This additional acceleration modifies the effect of gravity and hence modifies both the horizontal stress ratios and bed drag. Our results show that both the change in bed friction and the changes in horizontal stress ratios act together to deflect flowing granular material that encounters a ridge. A good example of such flow deflection is the split in the flow front tongue by the midchannel ridge shown in Figure 6.

[50] Bed shear stress, which is the dominant term decelerating the avalanche, is plotted in Figure 7f. Variations in flow velocity produce variations in vertical acceleration that directly couple to bed shear stress through equation (42). Comparison of Figures 7e and 7f illustrates how this coupling provides an important link between the vertical and horizontal components of acceleration of the avalanche as it encounters uneven terrain.

5. Conclusions

[51] Predicting the motion of granular avalanches across irregular, three-dimensional terrain poses challenges for model formulation, computation, and testing. We have developed and tested a depth-averaged computational model that is conceptually parsimonious as it invokes only conservation of mass and momentum and Coulomb friction to predict avalanche motion from initiation to deposition. Nonetheless, special care must be taken in honoring these principles as avalanches interact with irregular terrain. Use of a high-resolution finite volume method for computation of fluxes of mass and momentum, combined with a finite element method for computation of Coulomb stresses, provides numerical predictions that correspond well with analytical solutions and experimental data.

[52] In our model, significant computational advantages are realized through use of vertical cell boundaries. In contrast, most previous avalanche models have used curvilinear coordinate systems such that boundaries of computational cells are sloped at various angles with respect to the vertical and one another. This situation leads to variations in the gravity wave speed on individual cell boundaries and greatly complicates calculation of Riemann fluxes between cells. With vertical cell boundaries the gravity wave speed is constant on individual cell boundaries and varies only across the boundaries, simplifying volume integration of the governing conservation laws. Moreover, use of vertical boundaries facilitates linear decomposition of flux matrices and thereby facilitates accurate conservation of mass and momentum. However, because avalanches descend steep terrain, use of vertical cell boundaries necessitates that variable vertical accelerations must be taken into account in computation of basal and internal Coulomb stresses. We account for these accelerations by deriving an appropriate

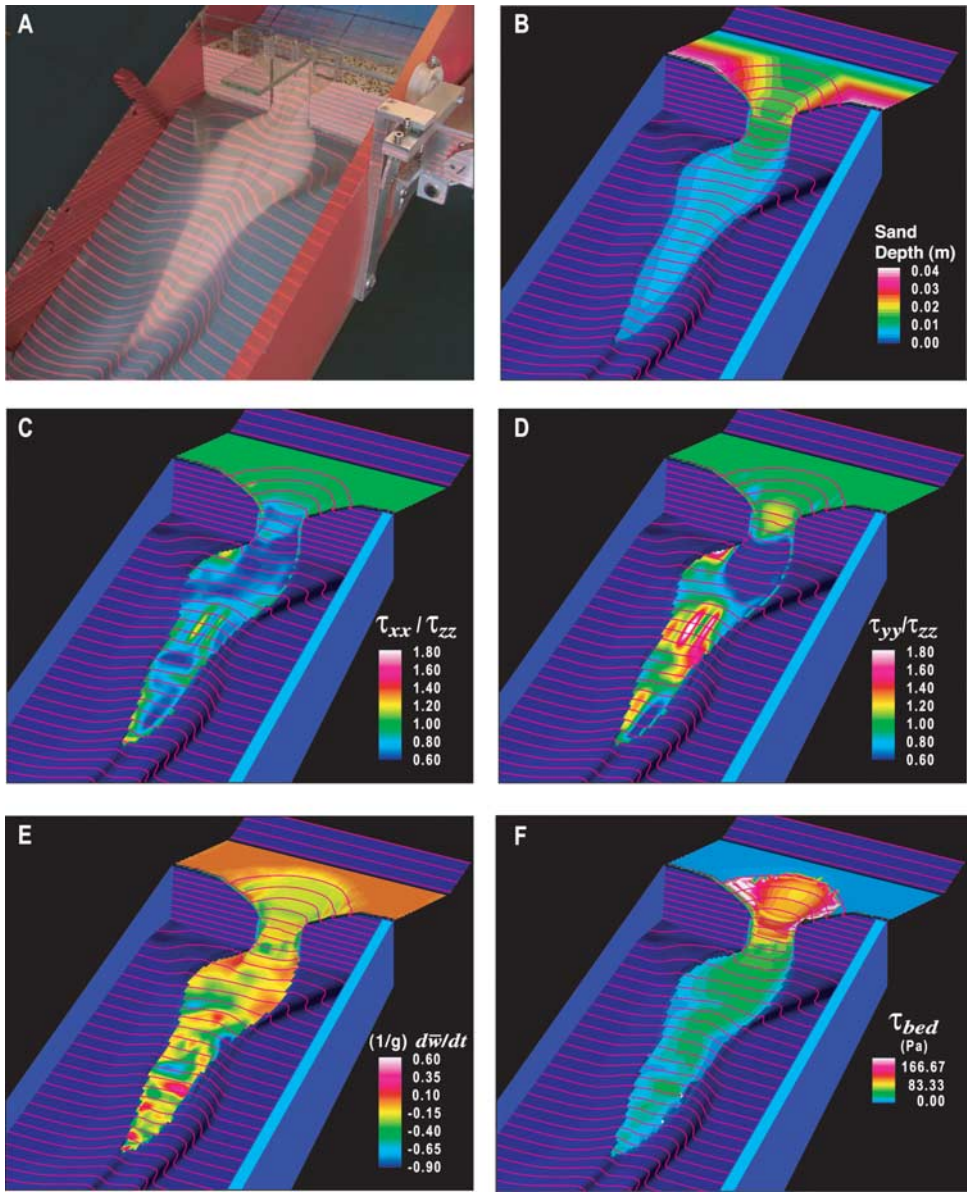

Figure 7. Oblique views of observed and computed avalanche behavior 0.31 s after avalanche release in experiment B of *Iverson et al.* [2004]. Lines running across the avalanche and bed surfaces are topographic contours at intervals of 0.5 cm. (a) Photograph of the physical experiment. (b) Computed avalanche thicknesses and velocities. (c) Computed magnitudes of downslope normal stresses. (d) Computed magnitudes of cross-slope normal stresses. (e) Computed magnitudes of the vertical acceleration. (f) Computed magnitudes of basal shear stress.

expression from the vertical momentum equation and inferring vertical velocities from kinematic constraints. Our results demonstrate that the magnitude of vertical accelerations may be comparable to that of gravity and that such accelerations have a pronounced effect on Coulomb friction and avalanche dynamics.

[53] Our model results illustrate a complex interplay between the basal shear stress and internal stresses that serves to deflect as well as focus avalanches as they interact with irregular terrain. The model predicts continuously varying distributions of all stress components, quite different from predictions of previous models and quite plausible at a continuum scale in granular masses that deform rapidly and pervasively.

[54] Comparison of our model results with applicable analytical solutions, conceptual experiments, and physical experiments demonstrates the predictive power of our formulation. For example, comparison with analytical dam break solutions illustrates the numerical accuracy of the model and the importance of including the total vertical acceleration in stress calculations. Comparison with a conceptual experiment involving a cylindrical column of sand that collapses to form a symmetrical cone illustrates the lack of spurious grid dependence in our mathematical and numerical formulation. Finally, and most importantly, comparison with detailed experimental data demonstrates that our model correctly predicts most aspects of avalanche motion across irregular, three-dimensional terrain. A com-

panion paper [*Iverson et al.*, 2004] provides details of these experimental tests.

Appendix A: Vertical Acceleration

[55] To help clarify the physical basis for employing the total vertical acceleration $g' = g + d\overline{w}/dt$, consider a simple, one-dimensional problem involving a uniform slab of material descending a frictionless slope uniformly inclined at the angle θ. Newton's second law indicates that the downslope velocity $\overline{p}$ of the slab obeys

$$d\overline{p}/dt = g\sin\theta. \tag{A1}$$

The horizontal (x) and vertical (z) components of the velocity ($\overline{u} = \overline{p}\cos\theta$ and $\overline{w} = -\overline{p}\sin\theta$) therefore obey

$$d\overline{u}/dt = g\sin\theta\cos\theta \qquad d\overline{w}/dt = -g\sin^2\theta. \tag{A2}$$

Equation (A2) implies that the vertical acceleration $-g\sin^2\theta$ reduces the effective weight of the slab (as measured by the vertical force exerted on the bed by the slab). Whereas the weight per unit of slab mass is g when the slab does not accelerate, the effective weight per unit of slab mass is $g - g\sin^2\theta$ during the acceleration described by equation (A2). Therefore to evaluate stresses in the slab (here assumed to occur exclusively in reaction to the slab's weight), it is convenient to define an effective vertical acceleration

$$g' = g\left[1 - \sin^2\theta\right] = g\cos^2\theta, \tag{A3}$$

which compensates for the reduced effective weight.

[56] Now consider how the same sliding slab problem is represented by the conservation equation for x momentum in our shallow flow model (7), wherein equations (7) and (16) reduce to

$$\int_A \rho\frac{d\overline{u}}{dt}dA = -\int_V\left[\frac{\partial\tau_{xx}}{\partial x}\right]dV = -\int_A\int_b^\eta\frac{\partial[k_x\rho g'(\eta - z)]}{\partial x}dzdA. \tag{A4}$$

In this simple case, $k_x = 1$ because strains are zero, and the x momentum equation implies that the only driving force is due to the horizontal stress gradient caused by the weight of the slab and the gradient in surface elevation η. If g' is constant and equal to gravity, then the x momentum equation (A4) reduces to

$$d\overline{u}/dt = -g(d\eta/dx) = g\tan\theta, \tag{A5}$$

which differs from the correct equation (A2). Equation (A5) is erroneous because it does not account for the reduction in horizontal stress and effective weight that results from the vertical acceleration of the slab. This error can be corrected by using g' to account for the effects of vertical acceleration. The appropriate value of g' can be obtained from equation (A2), in this special case, or from equation (13), which applies in all cases. For the special case considered here, reduction of equation (13) leads to

$$g' = g + \frac{d\overline{w}}{dt} = \frac{d}{dt}\left[\frac{1}{2}\overline{u}\left(\frac{\partial\eta}{\partial x} + \frac{\partial b}{\partial x}\right)\right] = g - \frac{d\overline{u}}{dt}\tan\theta. \tag{A6}$$

Replacement of g in equation (A5) by g' as defined in either equation (A3) or equation (A6) then yields, after some algebraic simplification,

$$d\overline{u}/dt = -g'(d\eta/dx) = g'\tan\theta = g\sin\theta\cos\theta, \tag{A7}$$

which recovers the correct result, as given by equation (A2).

Appendix B: Stresses Obtained From Basal Sliding

[57] The stresses obtained from drag on the bed are easily estimated in a coordinate system aligned so that one axis is normal to the bed, labeled below with primes. The components of shear stress are then obtained from the velocity and normal stress across the basal plane. In the primed coordinate system the drag stress is given by

$$\begin{pmatrix}\tau'_{xy}\\ \tau'_{yz}\\ \tau'_{xz}\end{pmatrix} = \begin{pmatrix}0\\ -\dfrac{\sqrt{v^2 + w_{\text{bed}}^2}}{\sqrt{u^2 + v^2 + w_{\text{bed}}^2}}\cdot\rho(g'\gamma_{zz'})h\cdot\tan\phi_{\text{bed}}\\ \dfrac{\sqrt{u^2 + w_{\text{bed}}^2}}{\sqrt{u^2 + v^2 + w_{\text{bed}}^2}}\cdot\rho(g'\gamma_{zz'})h\cdot\tan\phi_{\text{bed}}\end{pmatrix}, \tag{B1}$$

where the gravity term has components from weight and from inertia of debris flowing into the cell from upstream, as discussed in Appendix A, and the direction cosine $\gamma_{zz'}$ determines the fraction of the vertical acceleration that is directed normal to the basal plane.

[58] To estimate the effect of these stresses on each cell in the global system, the dipping shear plane is assumed to form one side of a tetrahedron, where the other three planes are oriented to the global system (Figure 1). For static balance the basal shear plane stress is related to stresses on the other three Cartesian planes by the transformation

$$\begin{pmatrix}\tau_{xx}\\ \tau_{yy}\\ \tau_{zz}\\ \tau_{xy}\\ \tau_{yz}\\ \tau_{xz}\end{pmatrix} = \begin{pmatrix}0&0&0&0&2mn&2nl\\ 0&0&0&0&2m'n'&2m'l'\\ 0&0&0&0&2m''n''&2m''l''\\ 0&0&0&0&(m'n''+m''n')&(n'l''+n''l')\\ 0&0&0&0&(mn''+m''n)&(nl''+n''l)\\ 0&0&0&0&(mn'+m'n)&(nl'+n'l)\end{pmatrix}\begin{pmatrix}0\\ 0\\ 0\\ \tau'_{xy}\\ \tau'_{yz}\\ \tau'_{xz}\end{pmatrix}, \tag{B2}$$

in which the l, m, n components of the matrix are direction cosines given by

$$\begin{pmatrix}x'\\ y'\\ z'\end{pmatrix} = \begin{pmatrix}l'&m'&n'\\ l''&m''&n''\\ l&m&n\end{pmatrix}\begin{pmatrix}x\\ y\\ z\end{pmatrix}, \tag{B3}$$

where z' in the primed system is orthogonal to the basal plane. The forces corresponding to these stresses are then added to forces generated by internal deformation to form a resultant stress that is corrected for the basal shear traction.

[59] **Acknowledgments.** The authors are indebted to Dan O'Connell and the U.S. Bureau of Reclamation for support of much of this work and for constant encouragement. We thank Joseph Walder, Randy Leveque, Kolomban Hutter, an anonymous reviewer, and the editors for careful reviews of the manuscript.

References

Abramowitz, M., , and I. A. Stegun (Eds.) (1964), *Handbook of Mathematical Functions with Formulas, Graphs, and Mathematical Tables*, 1046 pp., U.S. Dept. of Commer. Natl. Inst. of Stand. and Technol., Gaithersburg, Md.

Aris, R. (1962), *Vectors, Tensors, and the Basic Equations of Fluid Mechanics*, Prentice-Hall, Old Tappan, N. J.

Bagnold, R. A. (1954), Experiments on gravity-free dispersion of large solid spheres in a Newtonian fluid under shear, *Proc. R. Soc. London, Ser. A*, *225*, 49–63.

Coulomb, C. A. (1776), Su rune application des regles de maximis & minimus a quelques problems de statique, relatifs a l'architecture, in *Memoirs de Mathematique et de Physique*, *Presented at the Royal Academy of Sciences*, *1773*, pp. 343–384, Imp. R. Acad. Sci., Paris.

Denlinger, R. P., and R. M. Iverson (2001), Flow of variably fluidized granular masses across three-dimensional terrain: 2. Numerical predictions and experimental tests, *J. Geophys. Res.*, *106*, 553–566.

Desai, C. S., and H. J. Siriwardane (1984), *Constitutive Laws for Engineering Materials With Emphasis on Geologic Materials*, Prentice-Hall, Old Tappan, N. J.

Glicken, H. (1998), Rockslide-debris avalanche of May 18, 1980, Mount St. Helens volcano, Washington, *Bull. Geol. Surv. Jpn.*, *49*, 55–106.

Gray, J. M. N. T., M. Wieland, and K. Hutter (1999), Gravity driven free surface flow of granular avalanches over complex basal topography, *Proc. R. Soc. London, Ser. A*, *455*, 1841–1874.

Guinot, V. (2003), Riemann solvers and boundary conditions for two dimensional shallow water simulations, *Int. J. Numer. Methods Fluids*, *41*, 1191–1219.

Hubbard, M. E., and P. Garcia-Navarro (2000), Flux difference splitting and the balancing of source terms and flux gradients, *J. Comput. Phys.*, *65*, 89–125.

Hungr, O., and N. R. Morgenstern (1984), Experiments on the flow behavior of granular materials at high velocity in an open channel, *Geotechnique*, *34*, 405–413.

Hunt, M. L., R. Zenit, C. S. Campbell, and C. E. Brennen (2002), Revisiting the 1954 suspension experiments of R.A. Bagnold, *J. Fluid Mech.*, *452*, 1–24.

Hutter, K., and T. Koch (1991), Motion of a granular avalanche in an exponentially curved chute: Experiments and theoretical results, *Philos. Trans. R. Soc. London, Ser. A*, *334*, 93–138.

Hutter, K., M. Siegel, S. B. Savage, and Y. Nohguchi (1993), Two-dimensional spreading of a granular avalanche down an inclined plane part I. Theory, *Acta Mech.*, *100*, 37–68.

Iverson, R. M. (1997), The physics of debris flows, *Rev. Geophys.*, *35*, 245–296.

Iverson, R. M., and R. P. Denlinger (2001), Flow of variably fluidized granular masses across three-dimensional terrain: 1. Coulomb mixture theory, *J. Geophys. Res.*, *106*, 537–552.

Iverson, R. M., and J. W. Vallance (2001), New views of granular mass flows, *Geology*, *29*, 115–118.

Iverson, R. M., M. E. Reid, and R. G. LaHusen (1997), Debris flow mobilization from landslides, *Annu. Rev. Earth Planet Sci.*, *25*, 85–138.

Iverson, R. M., M. E. Reid, N. R. Iverson, R. G. LaHusen, M. Logan, J. E. Mann, and D. L. Brien (2000), Acute sensitivity of landslide rates to initial soil porosity, *Science*, *290*, 513–516.

Iverson, R. M., M. Logan, and R. P. Denlinger (2004), Granular avalanches across irregular three-dimensional terrain: 2. Experimental tests, *J. Geophys. Res.*, *109*, F01015, doi:10.1029/2003JF000084.

LeVeque, R. J. (2002), *Finite Volume Methods for Hyperbolic Problems*, 558 pp., Cambridge Univ. Press, New York.

Malvern, L. E. (1969), *Introduction to the Mechanics of a Continuous Medium*, Prentice-Hall, Old Tappan, N. J.

Mangeney, A., P. Heinrich, and R. Roche (2000), Analytical solution for testing debris avalanche numerical models, *Pure Appl. Geophys.*, *157*, 1081–1096.

Pudasaini, S. P., and K. Hutter (2003), Rapid shear flows of dry granular masses down curved and twisted channels, *J. Fluid Mech.*, *495*, 193–208.

Roe, P. L. (1981), Approximate Riemann solvers, parameter vectors, and difference schemes, *J. Comput. Phys.*, *43*, 357–372.

Savage, S. B., and K. Hutter (1989), The motion of a finite mass of granular material down a rough incline, *J. Fluid Mech.*, *199*, 177–215.

Savage, S. B., and K. Hutter (1991), The dynamics of avalanches of granular materials from initiation to runout, part I. Analysis, *Acta Mech.*, *86*, 201–223.

Savage, S. B., and R. M. Iverson (2003), Surge dynamics coupled to pore pressure evolution in debris flows, paper presented at the Third International Conference on Debris-Flow Hazards Mitigation, Davos, Switzerland, 13–15 Sept.

Toro, E. L. (1997), *Riemann Solvers and Numerical Methods for Fluid Dynamics*, 592 pp., Springer-Verlag, New York.

Voight, B., R. J. Janda, H. Glicken, and P. M. Douglas (1983), Nature and mechanics of the Mount St. Helens rockslide-avalanche of 18 May 1980, *Geotechnique*, *33*, 243–273.

Vreugdenhil, C. B. (1994), *Numerical Methods for Shallow Water Flow*, 261 pp., Kluwer Acad., Norwell, Mass.

Wieland, M., J. M. N. T. Gray, and K. Hutter (1999), Channelized free-surface flow of cohesionless granular avalanches in a chute with shallow lateral curvature, *J. Fluid Mech.*, *392*, 73–100.

Wood, D. M. (1990), *Soil Behavior and Critical State Soil Mechanics*, 462 pp., Cambridge Univ. Press, New York.

Zienkiewicz, O. C., and R. L. Taylor (1991), *The Finite Element Method*, vol. 2, *Solid and Fluid Mechanics*, 807 pp., McGraw-Hill, New York.

Zienkiewicz, O. C., and R. L. Taylor (2000), *The Finite Element Method*, vol. 1, *The Basis*, 689 pp., McGraw-Hill, New York.

R. P. Denlinger and R. M. Iverson, U.S. Geological Survey, 1300 SE Cardinal Court #100, Vancouver, WA 98683, USA. (roger@usgs.gov; riverson@usgs.gov)